ADVANCED FUNCTIONAL MATERIALS
www.afm-journal.de

X-Ray Tomoscopy Reveals the Dynamics of Ice Templating

Paul H. Kamm, Kaiyang Yin, Tillmann R. Neu, Christian M. Schlepütz, Francisco García-Moreno, and Ulrike G. K. Wegst**

Little experimentally explored and understood are the complex dynamics of microstructure formation by ice-templating when aqueous solutions or slurries are directionally solidified (freeze cast) into cellular solids. With synchrotron-based, time-resolved X-ray tomoscopy it is possible to study in situ under well-defined conditions the anisotropic, partially faceted growth of ice crystals in aqueous systems. Obtaining one full tomogram per second for ≈270 s with a spatial resolution of 6 µm, it is possible to capture with minimal X-ray absorption, the freezing front in a 3% weight/volume (w/v) sucrose-in-water solution, which typically progresses at 5–30 µm s^{-1} for applied cooling rates of $\dot{C}$ = 1–10 °C min^{-1}. These time and length scales render X-ray tomoscopy ideally suited to quantify in 3D ice crystal growth and templating phenomena that determine the performance-defining hierarchical architecture of freeze-cast materials: a complex pore morphology and "ridges", "jellyfish cap", and "tentacle"-like secondary features, which decorate the cell walls.

1. Introduction

Ice templating is the basis of structure formation when porous materials or cellular solids are manufactured by freeze casting, a processing technique based on the directional solidification of aqueous solutions and slurries. While also other solvents, such as camphene,[1] cyclohexane,[1d,2] *tert*-butyl alcohol (TBA),[1d,2] TBA-cyclohexane,[3] and naphthalene-camphor,[4] have been directionally solidified and the solvent-templated structures have been investigated, water-based systems continue to be the most widely used for materials processing. What remains little explored and understood in the case of all solvents, to date, are the complex dynamics of solvent crystal growth and templating during directional solidification. In this study, we focus on the dynamics of microstructure evolution during the directional solidification of aqueous systems. While highly anisotropic ice-crystal growth has, for some time, been hypothesized to play a critical role in the formation of the hierarchical architecture of freeze-cast materials, it remained largely unknown exactly how the honeycomb-like porosity and lamellar cell walls, which frequently are decorated with a range of unilateral surface features, are formed. X-ray tomoscopy now enables us to image in situ at high spatial and temporal resolution the mechanism of structure formation, including transient phenomena. Analyzing the tomoscopy data, we can determine, which of the unilateral features are templated by the slow faceted growth along the *c*-axis ⟨0001⟩ of the hexagonal ice-crystal, I_h, and which by the slightly anisotropic fast crystal growth along the preferred *a*-axis ⟨11$\bar{2}$0⟩ and prism *t*-axis ⟨1$\bar{1}$00⟩, directions which are both characterized by atomically rough ice-water interfaces.

P. H. Kamm, T. R. Neu, F. García-Moreno
Institute of Applied Materials
Helmholtz-Zentrum Berlin für Materialien und Energie
Hahn-Meitner-Platz 1, 14109 Berlin, Germany
E-mail: garcia-moreno@helmholtz-berlin.de

P. H. Kamm, T. R. Neu, F. García-Moreno, U. G. K. Wegst
Institute of Materials Science and Technology
Technische Universität Berlin
Hardenbergstr. 36, 10623 Berlin, Germany
E-mail: u.wegst@northeastern.edu

K. Yin, U. G. K. Wegst
Thayer School of Engineering
Dartmouth College
15 Thayer Drive, Hanover, NH 03755, USA

K. Yin, U. G. K. Wegst
Department of Physics
Northeastern University
360 Huntingdon Avenue, Boston, MA 02115, USA

K. Yin
Department of Microsystems Engineering
University of Freiburg
Georges-Köhler-Allee 078, 79110 Freiburg, Germany

C. M. Schlepütz
Swiss Light Source
Paul Scherrer Institute
Forschungsstr. 111, 5232 Villigen, Switzerland

The ORCID identification number(s) for the author(s) of this article can be found under https://doi.org/10.1002/adfm.202304738

DOI: 10.1002/adfm.202304738

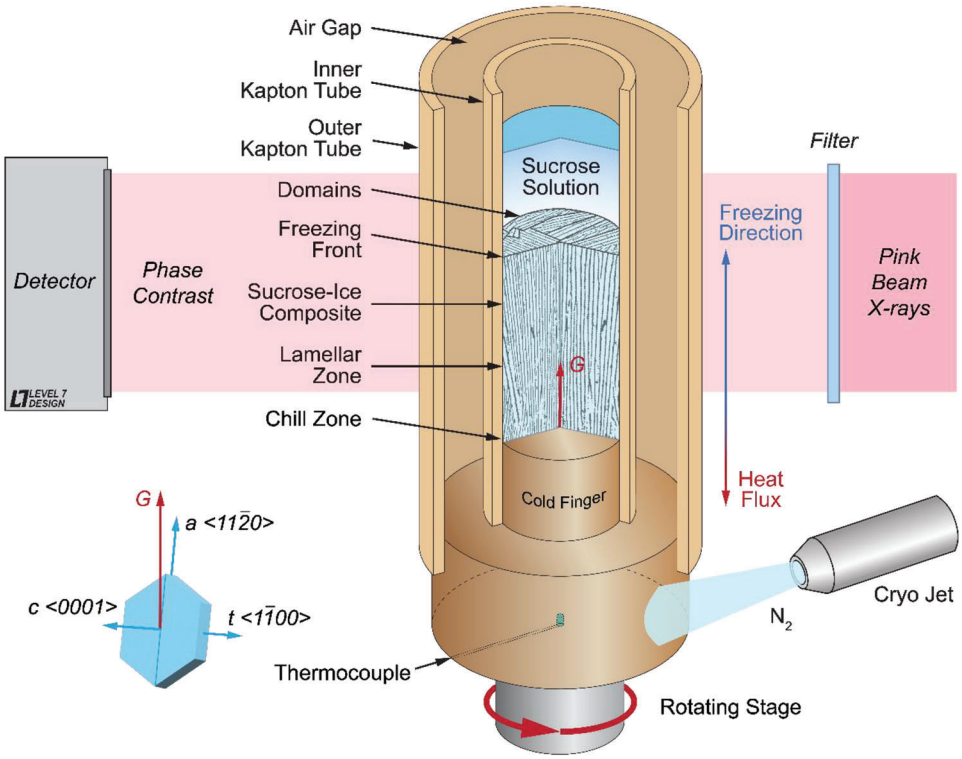

Figure 1. Schematic of the freeze casting process. Ice crystals typically nucleate on the top surface of the cold finger, which seals the mold bottom. The fine, equiaxed grains of the textureless chill zone grow competitively in the general direction of maximum heat flow, which is imposed by the applied thermal gradient, *G*. As the freezing front progresses, a phase separation into pure ice crystals and solute occurs. Dendritic ice crystal growth ensues with the fastest crystal growth direction, the *a*-axis ⟨11$\bar{2}$0⟩, closely aligned with the thermal gradient, thereby forming the lamellar structure of each grain.[10] During this crystal growth, the solute is upconcentrated and ice-templated in the interdendritic spaces until vitrification occurs.

Additionally, we can observe, which role secondary instabilities play in the formation of cell wall surface features, such as "ridges", "jellyfish caps", and "tentacles".[12] We can also quantify ice-crystal growth velocities, both volumetric and parallel to the crystallographic axes, to correlate these to the ice-crystal growth phenomena which we observe. An important advantage that X-ray tomoscopy offers over post mortem and also state-of-the-art simulation techniques, which for computational reasons are limited to small sample volumes of a couple of hundred micrometer side length and corresponding timespans, is that the dynamics of the structural evolution can be monitored over several minutes, and that a sample volume of several tens of cubic millimeters can be studied.

When aqueous solutions and slurries solidify, a phase-separation occurs. Water solidifies into pure ice and the dissolved polymer(s) and/or suspended particles are upconcentrated between the growing ice dendrites, which template the second phase composed of polymers or particles, or a composite of both.[5] What makes freeze casting attractive as a manufacturing process is that complex hybrid materials with hierarchical architectures and remarkable properties can be made for uses that range from biomedical[6] to energy applications.[7] Here, we focus on binary sucrose-in-water solutions to quantify in situ with high temporal and spatial resolution how the partially faceted, anisotropic, nonequilibrium, and diffusion-limited ice-crystal growth templates unique and unilateral performance-defining structures, when morphological instabilities form on the atomically rough portions of the growth fronts.[6e,8] To facilitate a quantitative observation of the ice-crystal growth dynamics in 3D, we require a powerful in situ imaging technique: X-ray tomoscopy.

X-ray tomoscopy is newly available for the continuous imaging of complex dynamic processes[9] and ideally suited for the quantitative analysis of directional solidification. We have coined the term "tomoscopy" for time-resolved imaging with continuous sample illumination and data acquisition rates of currently up to 1000 tomograms per second (tps), and a data acquisition duration chosen ideally suited to capture the dynamics of the system under study, while minimizing motion artifacts due to sample evolution.

Figure 1 illustrates the authors' miniature freeze casting system custom-designed for high resolution X-ray tomoscopy of directional solidification at the TOMCAT beamline of the Swiss Light Source at the Paul Scherrer Institute, Switzerland. The advantages offered by X-ray tomoscopy are considerable[9] as this technique uniquely facilitates the quantitative analysis of key parameters of the dynamic solidification process. Parameters include freezing front velocity, crystal growth velocities in individual crystallographic directions, and both the local and global structural evolution at high resolution. Noteworthy is that also otherwise elusive transient events are captured.

The volume-rendered 3D datasets of the samples can be virtually sectioned and segmented in any direction and orientation so that their structural evolution can be observed both site-specifically and in relation to the global sample orientation. The orientation and alignment of individually growing ice crystals, as well as the formation and evolution of the various ice-templated features can be analyzed in detail. Most importantly, X-ray tomoscopy makes it possible to study the entire life cycle of transient features, from their appearance and further evolution to their disappearance; such phenomena cannot be observed post mortem because typically not even traces of them are preserved in the final freeze-cast material.

Best suited for a fundamental study of the complex and coupled solidification phenomena that occur during freeze casting are binary material systems. As model system, we selected a sucrose-in-water solution, for which the phase diagram and fundamental properties, such as diffusion coefficients, are known.[8a,10,11] Such a system is advantageous, because it can also be simulated using, for example, phase-field methods to complement the experiments.[12] For imaging, we chose X-ray tomoscopy with phase contrast, because X-rays penetrate the model system easily, and partial or full phase contrast enables the observation also of systems, in which solution, solvent, and solute, such as our model sucrose-in-water solution, have similarly optical properties and low atomic numbers.[13] Finally, tomoscopy offers the required spatio-temporal resolution to capture the dynamics of ice crystal growth phenomena in 3D.[9]

2. Results

2.1. X-Ray Tomoscopy of the Freeze Casting Process

The directional solidification of a 3% w/v aqueous sucrose solution held in a 2 mm diameter, 30 mm long Kapton tube was successfully imaged in situ by X-ray tomoscopy, while applying a defined thermal gradient to the solution with the custom-made miniature freeze-casting system shown in Figure 1. To confirm that the solidification process was not affected by the energy entry associated with X-ray exposure, the final microstructure of the 2 mm diameter in situ samples was compared with the microstructures of a standard 20 mm diameter sample = of the same composition that had first been freeze cast ex situ, then imaged with a desktop X-ray tomography system (Figure S1, Supporting Information). Both samples exhibited the same structural dimensions, such as lamellar spacing and cell wall surface features (Table S1, Supporting Information), thereby confirming that the experimental parameters chosen for continuous in situ imaging by X-ray tomoscopy did neither alter the directional solidification process nor led to the formation of artifacts.

Another question which arises is whether the high-velocity sample rotation affects the solidification process. The radial acceleration, a_r, and forces generated, $F_r = ma_r$, which a sample experiences, increases with sample radius, r, and rotation frequency, f, as $a = 4\pi^2 f^2 r$. Both sample radius and rotation frequency thus need to be chosen so that the sample is not affected beyond an acceptable threshold.[9a,b] In our case of directional solidification of a sucrose solution with $r = 1$ mm imaged at $f = 1$ Hz, the radial acceleration is $a = 0.04$ m s^{-2} at maximum distance from the rotation axis, thus negligibly small. Paralleling the analysis for X-ray energy exposure effects, we compared samples frozen without and with rotation, and found no difference also for these.

The spatio-temporal evolution of both the ice crystal growth and the solute structure can be studied in detail by volume-rendering the in situ X-ray tomoscopy of the directional solidification of the 3% w/v sucrose-in-water solution (**Figure 2**a). The resulting image sequence (Figure 2a, see also Video S1, Supporting Information) shows that, once the ice phase (blue) has nucleated at the copper mold bottom, a phase separation occurs and dendritic ice crystal growth templates the solute phase (red), which is increasingly upconcentrated in the interdendritic spaces. Both the freezing front position and the corresponding freezing front velocity, averaged for the entire sample cross-section, are plotted versus time in Figure 2b. The graph shows that the freezing front velocity, which is the rate at which the freezing front height increases, slows with time.

Additionally, Figure 2b reveals significant fluctuations in the freezing front velocity for the entire 220 s of the solidification process studied; we analyze these fluctuations in detail below. The longitudinal and transverse sample cross-sections shown in Figure 2c illustrate that the sample is composed of several grains or domains, each of which has a lamellar structure. The cross-sections also reveal the alignment of lamellae and domains with respect to the mold axis, which parallels the applied thermal gradient, G (Figure 1).

2.2. Structure-Processing Correlations

Video S1 (Supporting Information) of the progression of directional solidification illustrates the dynamics of the structure formation process, which defines the overall architecture of the final sucrose scaffold. The video highlights the anisotropy in ice crystal growth[12] and shows, how domains of different angles of alignment with respect to the thermal gradient, G, compete during the grain elimination phase, thus which of the domains are gradually overgrown and eliminated, and which dominate and survive as the freezing front progresses. The video also shows how the cross-sectional size and shape of the domains change with time. Additionally, we observe that thickness and width of each of the lamellar ice dendrites, which define the short, S, and the long, L, pore axis of the final scaffold after freeze drying, respectively, increase with increasing height. The increase in thickness with height is due to a decreasing local cooling rate with mold height,[12] while the growth in lamellar width is constrained by neighboring domains and likely also affected by the thermal contraction of the mold (Figure 2c and Video S1, Supporting Information).

Summarized and color-coded in the sample cross-sections of **Figure 3**a is the alignment of the lamellae within a domain to highlight how well adjacent domains can be aligned with one another. The stack of six equidistant (540 µm) sample sections in Figure 3b reveals how the number of domains and their cross-sectional shape changes with increasing height in the mold. Figure 3c illustrates two neighboring domains with similar crystal and lamellar orientation extending along the entire sample height, the inner gradually overgrowing the outer.

How lamellae within different domains align, and how domains are oriented with respect to one another and the mold axis

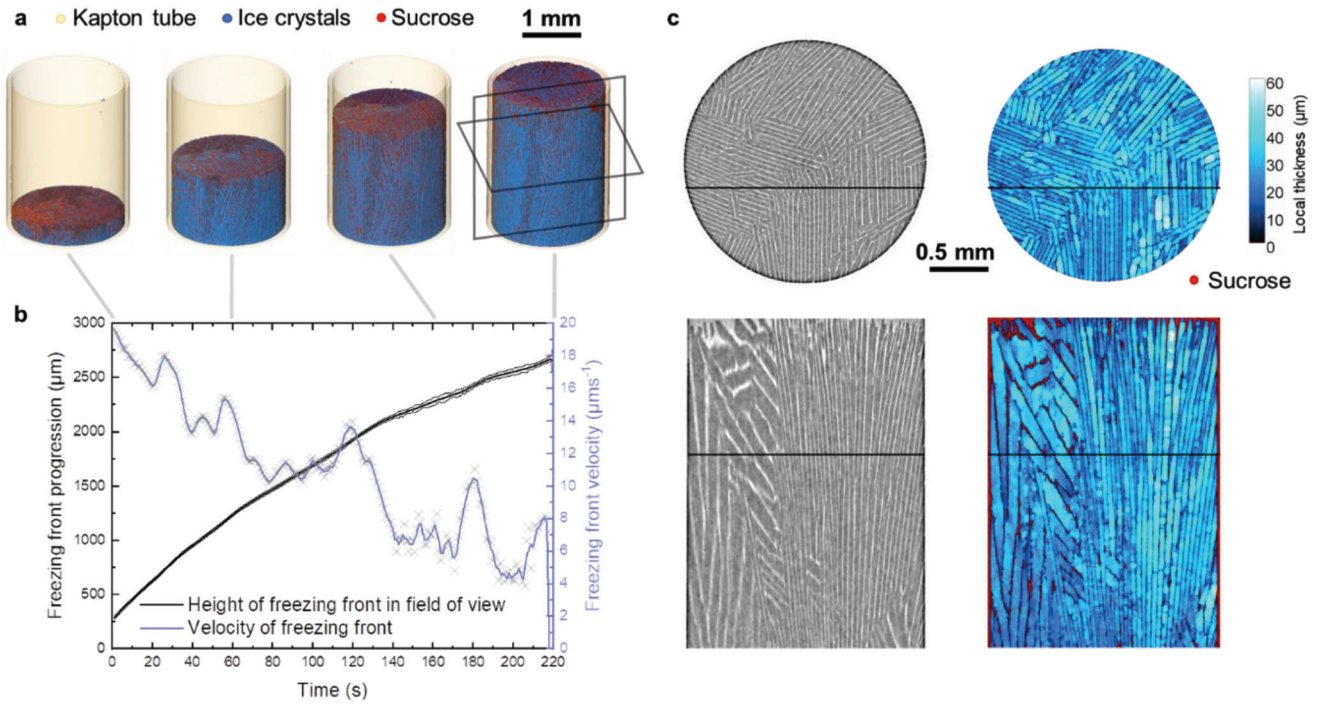

Figure 2. a) 3D rendered tomograms at different times showing ice crystals in blue, sucrose in red, and Kapton tubes in yellow. To clearly show and highlight the solidification front, the mixed liquid phase was masked out. b) Average freezing front progression along the mold height, *H*, and the corresponding average freezing front velocity over time. c) Vertical and cross-sectional slices of the sample structure at 220 s at the positions marked by black frames in a show both in grey-scale and false color (ice crystal thickness in blue shades, sucrose in red) the lamellar structure of the directionally solidified material.

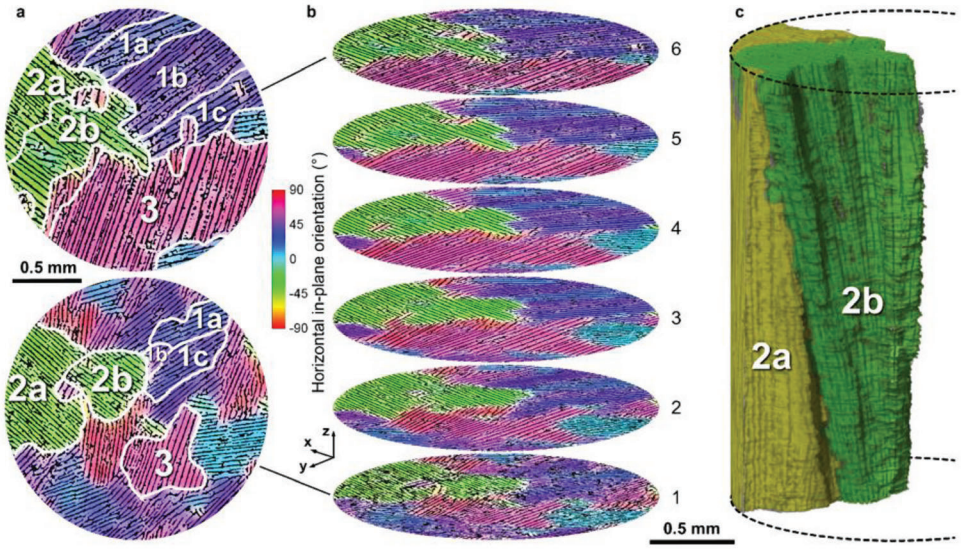

Figure 3. a) Top views of layers 1 and 6, respectively, highlight how closely aligned neighboring grains can be in their in-plane lamellar orientation. White lines and numbers denote selected domains. The colors indicate the angle enclosed between the lamellae of the respective domain and an imaginary horizontal axis parallel to the equator of the top views of (a), i.e., domains (1a–c) and (2a,b) are misaligned with each other by only a few degrees, whereas domains 1, 2, and 3 exhibit distinctly different lamellar orientations with respect to one another. b) A stack of cross-sections at six equidistant heights illustrates domain evolution and competitive growth. c) Competitive growth of two neighboring domains (2a,b); the domain best aligned with the slightly fanning actual thermal gradient in the mold overgrows the other. The sucrose cell walls in (a) and (b) are colored black.

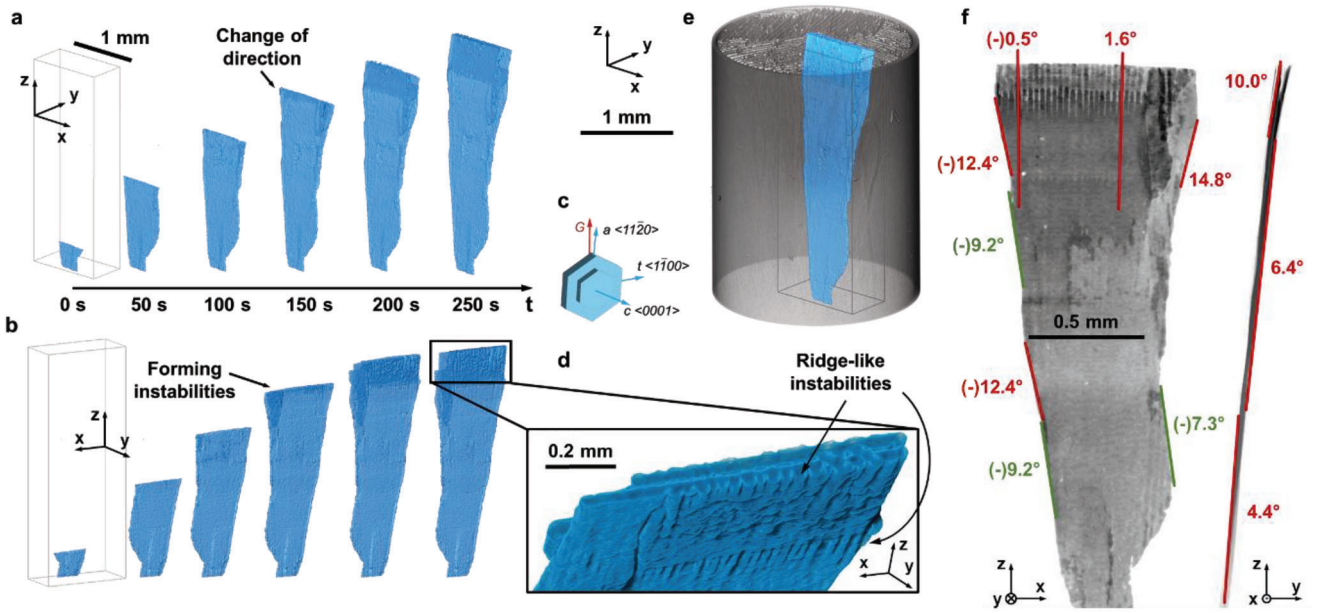

Figure 4. Shown are 3D rendered tomograms illustrating anisotropic crystal growth. a) Longitudinal growth parallel to the *a*-axis ⟨11$\bar{2}$0⟩ is faster than the lateral b) parallel to the *t*-axis ⟨1$\bar{1}$00⟩, as shown here for a slightly inclined (4.4° to 10°) ice lamella observed for 250 s. Instabilities form at ≈150 s at a sample height of ≈220 µm; it is followed by a change in crystal growth direction that becomes clearly evident at $t > 150$ s. c) Schematic of an ice crystal, such as depicted in (b), indicating its crystallographic directions and slightly exaggerated orientation with respect to the applied thermal gradient, *G*. d) A close-up view of the "ridge"-like instabilities on the ice crystal reveals that they point toward the cold side (bottom) of the mold. e) The fully grown ice lamella and its location and orientation within the sample. f) Development of angles of crystal growth and incline on a projection of the single lamella with height up to 2387 µm.

(and applied thermal gradient), is summarized in Figures 3a–c, respectively. The stack of six equidistant (540 µm) sample sections in Figure 3b illustrates how significantly both the cross-sectional shape and the number of domains change with height. Figure 3c shows two neighboring domains with similar domain and lamellar orientation extending along the sample height, the inner gradually overgrowing the outer. Figures 3a–c also highlight how closely correlated adjacent domains can be in crystallographic orientation, as indicated by lamellar and domain alignment.

2.2.1. Ice Crystal Growth and Orientation

From experimental analysis by cryo-EBSD[10] and theory[12,14] we know that, during competitive growth and grain selection, those grains with the fastest crystal growth direction (*a*-axis ⟨11$\bar{2}$0⟩) most closely aligned with the thermal gradient win. The winning grains define the freezing front velocity, as well as the domain size and their lamellar orientation.[10] Imaging the crystal growth dynamics by tomoscopy and analyzing the resulting data sets, we can now not only measure fluctuations in the freezing front velocity, but also quantify the anisotropy of ice crystal growth along the different crystallographic axes (**Figure 4**c).

The *a*-axis ⟨11$\bar{2}$0⟩ grows approximately at the speed of the freezing front. The *t*-axis ⟨1$\bar{1}$00⟩, which determines the ice crystal width, grows, when unconstrained, almost as fast as the *a*-axis, here a little more slowly. And the *c*-axis ⟨0001⟩, which defines the thickness of the ice lamellae, grows the slowest, about two magnitudes more slowly than the *a*-axis ⟨11$\bar{2}$0⟩.

Extracting one ice lamella from one of the central domains depicted by data segmentation, as shown in Figure 4 and Video S2 (Supporting Information), we can analyze both the ice crystal growth parameters and the resulting structural evolution in unprecedented detail. We observe that not only the lamellar thickness and width increase with height (Figure 4a,b; Figure S2, Supporting Information), but that also the crystal growth direction changes at $t = 200$ s, and that secondary instabilities form on the lamellar ice crystals (Figure 4b,e).

The analysis of $n = 80$ ice crystals with "ridges" in $m = 12$ domains (Figure S3, Supporting Information) confirms the observations made in earlier post mortem analyses of freeze-cast polymer scaffolds,[6e,8a,10,15] namely that the secondary instabilities on the ice crystals stably form unilaterally on the faces oriented downward toward the cold end of the mold. On 71 out of 80 crystals the instabilities clearly pointed downward, on the others, the angles of incline with the mold axis were too small to make a clear distinction; this also in the light of the fact that the actual local thermal gradient may enclose a small angle (<1°) with the mold axis.

As a result, the ice-templated "ridges" on the solute scaffold walls face toward the warm end. Additionally, we observe that in parallel to the crystal width and thickness also the height and spacing of these secondary instabilities increase with height in the mold (Table S1 and Figure S3, Supporting Information). Investigating the crystal incline with respect to the applied thermal gradient, we notice that the angle increases from 4.4° at the bottom to 10° at the top of the 2400 µm long extracted ice lamella; the angles of the crystal's lateral incline follow those of the neighboring domains (Figure 4f).

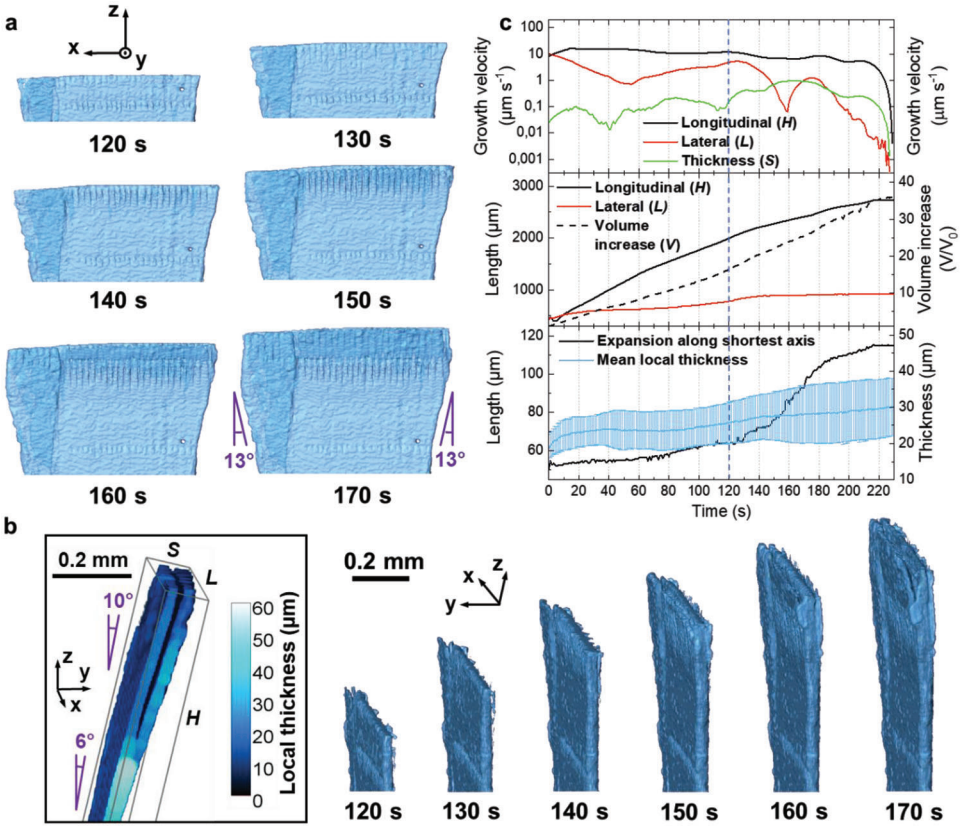

Figure 5. a) 3D rendered tomograms of a slightly inclined ice lamella with b) a lateral view of crystal growth and instability development. Instabilities form at 150 s followed by a change in crystal growth direction (from 6° to 10° to the *z*-axis) accompanied by a lamellar split into two. c) Longitudinal, lateral, and thickness growth velocities, as well as the volume increase plotted against time, highlighting the highly anisotropic, faceted crystal growth of the ice lamella. Dimensions of the respective quantities are indicated on the left and right *y*-axes of the graph, respectively.

2.2.2. Anisotropic Crystal Growth

Of considerable interest for an analysis of anisotropic ice crystal growth is the ability to measure and compare the crystal growth velocities parallel to the *a*-axis $\langle 11\bar{2}0 \rangle$, the *t*-axis $\langle 1\bar{1}00 \rangle$, and the *c*-axis $\langle 0001 \rangle$, which determine the ice crystal's extension in length, *H*, width, *L*, and thickness, *S*, respectively. Plotting crystal growth velocities versus time in **Figure 5**c, we note not only the expected differences in longitudinal versus lateral growth rates, but additionally significant fluctuations in freezing front velocity along all three crystal growth directions, while the ice crystal volume increases at an almost constant rate. Investigating the lamellar shape evolution in parallel, we discover that longitudinal, lateral, and thickness growth accelerations and decelerations correlate to the dimensional changes of the ice lamella shown in Figures 4 and 5. For example, longitudinal growth always slows when the ice crystal expands laterally or in thickness, and when instabilities form; and longitudinal growth accelerates, again, when the crystal splits into two.

2.2.3. Instability Formation and Solute Templating

Instability formation on the ice crystal face oriented toward the mold bottom is observed for the first time at ≈17 s with a wavelength of ≈18.11 ± 1.09 µm (**Figure 6**; Figure S3a, Supporting Information), at 47 s with a wavelength of ≈19.92 ± 1.10 µm (Figure S3b, Supporting Information), then again at 128 s (Figures 5 and 6) with a larger wavelength of ≈23.79 ± 1.30 µm (Figure S3c). These instabilities can evolve into different shapes and template in the solute phase structural features, such as "ridges" parallel to the direction of solidification (Figures 5 and 6, Supporting Information). From time to time, "jellyfish caps" or "jellyfish-cap arrays" on the solute cell walls indicate that one or more ice crystal instabilities have been eliminated, respectively (Figures 5a and 6b, Supporting Information).[8b,12]

We observe instability formation on the ice lamella for a third time at ≈160 s (Figures 5 and 6). This time, the instabilities are thicker than those observed at 130 s, but spaced at only a slightly increased distance. Also, these thicker instabilities template, as before, regularly spaced "ridges." When the ice crystal tip splits into two parallel ice lamellae at ≈165 s, "tentacle"-like solute features, which are effectively "pinched-off ridges" (blue box), form as part of a second "jellyfish-cap array" (Videos S2 and S3, Supporting Information). Observing crystal growth and ice templating in real time in this dynamic study, allows us to make several other important observations and discoveries, which cannot be made by traditional static, post-mortem material analysis.

The first discovery is that initially both faces of the ice lamella perpendicular to the *c*-axis form an instability array with highly

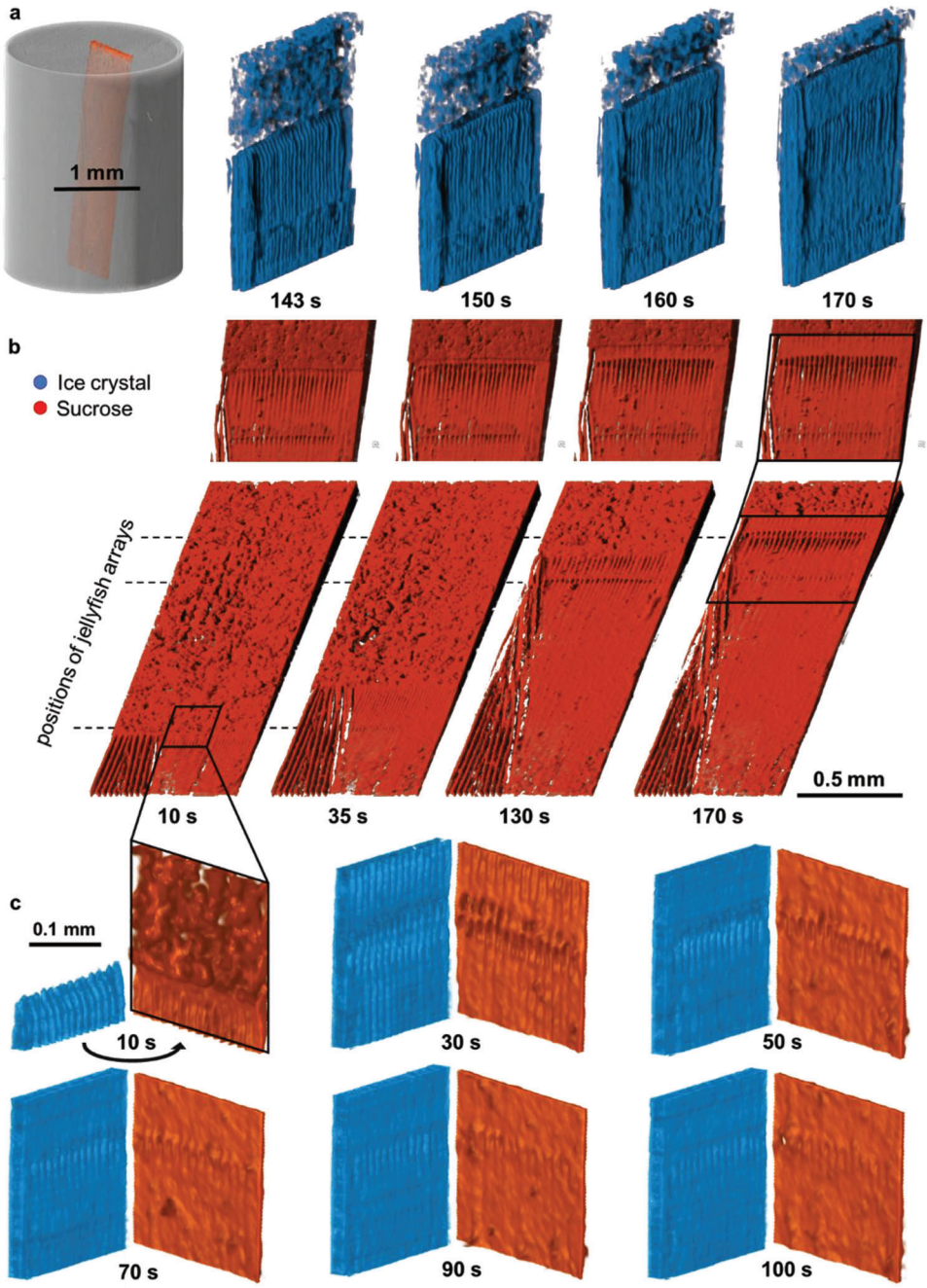

Figure 6. a) 3D rendered tomograms of the ice phase evolution from 143 to 170 s. b) The temporal evolution of the sucrose phase structure from 10 to 170 s. The temporal evolution of the "jellyfish-cap array" illustrates how crystal growth and volumetric expansion of the ice phase sharpen the structural features and pull the "jellyfish-cap array" along parallel to the direction of solidification. c) The direct comparison of the ice-template (blue) and the templated sucrose (red) from 10 to 100 s illustrates the formation of transient features, such as a "jellyfish-cap array," whose features become less prominent as the ice crystal growth increasingly dries the solute phase.

parallel features; these features are shallow on one side and more pronounce on the opposite side (Figure 5c). However, following the evolution of these features, we find that only the more pronounced instabilities on the crystal face oriented toward the cold end of the mold are stable (Figures 2, 5, and 6). This is the reason for the observation of unilateral structural features in ice templated materials. Because the ice-templated instabilities shrink only minimally during lyophilization, they are typically preserved in size and shape, and clearly visible, when scaffolds are imaged in the lyophilized state.

Another important observation we could only make in our 3D dynamic study is the formation, evolution, and disappearance of

entirely transient features (Video S4, Supporting Information). Figure 6c illustrates this phenomenon for both the ice and the solute phase. At 10 s, ice crystal instabilities start to form, templating in the solute phase features, such as "ridges" and a "jellyfish-cap array." At 30 s, we see that these different features first grow and increase in height and thickness, at 50 s we notice that the features start to become less pronounced, further shrinking to smaller sizes at 70 and 90 s, to result in features at ≈100 s that are considerably flatter and less defined than at 10 s.

Finally, we note another important phenomenon contributing to the hierarchical structure formation in the ice-templated scaffold: the effect of mechanical forces that act on the increasingly viscous solute phase, on the one hand during the ice-water phase transformation, which is accompanied by a volumetric expansion of ≈9%, and on the other when the ice crystals grow. The volumetric expansion causes interdendritic shear flow and contributes to convection phenomena ahead of the freezing front, both of which determine alignment and preferential orientation of solute molecules in solutions and particles in slurries.[16] In parallel, the growing ice crystals push along and stretch the upconcentrated solute phase parallel to the crystal growth directions, which becomes particularly apparent in the fastest growing direction of solidification. The positional change of the "jellyfish-cap array" parallel to the freezing direction, shown in Figure 6b,c and Video S2 (Supporting Information), illustrates this.

3. Discussion

3.1. Tomoscopy for the Quantification of Dynamic Structure Formation

The unprecedented wealth of quantitative and detailed qualitative information on ice crystal growth and ice templating obtained in this study of directional solidification highlights the considerable advantages that X-ray tomoscopy offers for the study of the complex dynamics of structure formation during directional solidification. Critical for the experimental success of this study of the freeze casting process was the choice of the binary water-sucrose model system, which made it possible to study ice crystal growth during directional solidification without the added complications of, for example, particle sedimentation, particle-particle and particle-freezing-front interactions, and particle-induced enhanced X-ray absorption and heating. All these particle-related effects contribute to structure formation phenomena and, additionally, to undesirable artifacts related to thermo-solutial convection and freezing-melting-refreezing cycles of the system under study,[17] which can affect and obscure fundamental ice-crystal growth and ice-templating phenomena.

Imaging the solidification process of the water-sucrose system was facilitated by synchrotron-based X-ray tomoscopy with phase contrast, which allowed us to observe in situ and under well-defined experimental conditions the anisotropic, partially faceted growth of ice crystals in 3D bulk rather than in thin, 2D samples. This is important, because sample imaging by light or confocal microscopy,[18] and also by X-ray radioscopy[17,19] is limited to thin, 2D material films, which frequently are only 50–200 µm thick. The in 2D experiments typically used Hele-Shaw cells confine crystal growth to thin film systems to reduce convection but, at the same time, add boundary effects which are absent in 3D. Hele-Shaw cells also limit structural information and resolution, because morphological features often overlap in 2D. For these reasons, phenomena observed and results obtained in 2D do not necessarily resemble those captured in 3D in a bulk sample, so that the potential to predict structure formation in 3D from 2D data is limited. The in 3D frequently observed formation of ice crystal instabilities and resulting ice-templating surface features, such as "ridges", "jellyfish cap"-like features, and "tentacles", for example, cannot be discerned in 2D.

3.2. Structure-Processing Correlations

3.2.1. Ice Crystal Growth Velocity and Dimensions

With X-ray tomoscopy we could observe in situ mechanisms of structure formation by ice templating, which result in the typical polydomain structure of freeze-cast materials, in which neighboring domains can be closely aligned with one another. Due to phase separation, each of the domains is composed of several closely aligned hexagonal ice prisms, also termed ice lamellae, whose *a*-axes $\langle 11\bar{2}0\rangle$ are closely aligned with one another and the applied thermal gradient.[10] An analysis of the lamellar angle of incline with the *z*-axis of the mold, which parallels the direction of applied thermal gradient, *G*, reveals that the angles of incline of most lamellae and domains fall within an angle range of 4.4° to 10°.

The lamellae exhibit a partially faceted, anisotropic ice crystal growth due to different molecular mobilities at the crystal-liquid interfaces.[12] X-ray tomoscopy enabled us to experimentally quantify this anisotropy of crystal growth in detail (Figure 5c). Fastest crystal growth is observed on the six molecularly rough secondary prism facets $\{11\bar{2}0\}$, because water molecules can attach everywhere, closely followed by the also molecularly rough six prism facets $\{1\bar{1}00\}$, which grow by a mixed growth mechanism.[20] In contrast, the layer-by-layer crystal growth of the molecularly smooth basal facet {0001} is, with a factor of 10–100, considerably slower.

The 3D continuous in situ imaging by tomoscopy additionally enabled us to determine the cause of the intriguing fluctuations in the longitudinally freezing front velocity (Figures 2b and 5c). Quantifying and correlating the crystal growth velocities parallel to the three crystal growth directions $\langle 11\bar{2}0\rangle$, $\langle 1\bar{1}00\rangle$, and ⟨0001⟩ (Figure 5c), we discovered that all three crystal growth velocities fluctuate, but not the volumetric crystal growth rate. The velocity parallel to the fastest crystal growth direction $\langle 11\bar{2}0\rangle$ decreases when the growth velocities of one or both of the crystal growth directions perpendicular to it increase (Figure 5c). These lateral growth events correspond to the formation of instabilities and the splitting of an ice lamella (Figure 5b).

The volumetric crystal growth rate remains almost constant; it only very gradually decreases with time and the corresponding freezing front height in the mold, in parallel to the decrease in the local cooling rate, $\dot{C}$, with mold height, *H* (Figure S4 and Table S2, Supporting Information). The local cooling rate decreases, because no true steady state conditions can be reached by applying a constant temperature to one mold end, while the other remains open, to create the temperature gradient that serves as the driving force for solidification.[5e,21] Additionally, a thermal diffusion lag

and thermal transfer through the open mold end and walls contribute to this effect. The thermal lag is defined by the thermal diffusivity of the mushy zone, which is composed of alternating ice lamellae and increasingly upconcentrated interlamellar solute (Figure 1), and increases in length with increasing height along the mold (Figure S5, Supporting Information).

3.2.2. Ice-Templated Cell Wall Surface Features

In addition to the anisotropic, faceted crystal growth phenomena that control both pore size and geometry after lyophilization,[6b–f,15,22] also the performance-defining, unilateral cell wall surface features like "ridges"[8b] and "jellyfish caps"[12] are of great experimental and fundamental interest. A close inspection of the directionally solidifying ice crystals (Figures 4–6; Figure S6, Supporting Information) reveals the anisotropy of ice crystal growth. The ice crystal tips, which form the freezing front, possess one smooth and one rough crystal face. The smooth ice crystal facets predominantly face toward the warm top end of the mold, and the rounded "rough" faces point toward the cold mold bottom.[12] All of the unilateral instabilities form on the rough ice crystal face to then template a rich variety of unilateral features on the solute cell walls.[6e,8b,15]

Recent phase field simulations of the directional solidification of 3% w/v sucrose in water solutions, thus the same materials system as that used in our experiments, here, provide further detail for the mechanisms of structure formation in binary water mixtures containing small solutes obeying Fickian diffusion.[12] The unilateral smooth facet at the crystal tip is formed by slow faceted ice crystal growth along the *c*-axis combined with a small misorientation of the basal plane with respect to the thermal gradient, *G*. The rough crystal face results from a weak six-fold anisotropy of the interface free-energy in the basal plane and fast crystal growth along these growth direction.[12] Diffusion-controlled cellular primary instabilities that form on the rough side of the ice crystals template regularly spaced "ridges." The more complex features, such as "jellyfish caps" and "tentacles" are templated by secondary instabilities that evolve from the cellular instabilities.[12]

Experimentally we observe that, from time to time, the "ridge" spacing decreases and the sucrose solute becomes so significantly upconcentrated at the freezing front, that a "jellyfish cap"-like solute feature forms (dashed line in Figure 6), which traps and eliminates one or more secondary instability and is followed by an adjustment in cellular spacing. When the instabilities are very closely spaced, tube-like channels form which template "jellyfish tentacles" these can be partially or fully detached from the otherwise smooth cell wall that supports it. "Jellyfish tentacles" tend to form below the "jellyfish caps." Intriguing is the observation of the appearance, evolution, and disappearance of a "jellyfish-cap array" (Figures 5 and 6), which highlights the value of tomoscopy as a dynamic characterization technique, because, in contrast to static and post mortem techniques, it can also capture transient events.

4. Conclusion

X-ray tomoscopy with phase contrast at one tomogram per second reveals the complex dynamics of ice crystal growth and microstructure formation by ice-templating, which form the basis of the freeze casting process and occur when aqueous solutions or slurries are directionally solidified into cellular solids. Using water-sucrose as our binary model system, we quantify the anisotropic, partially-faceted crystal growth over sample lengths that include the liquid phase, the mushy zone, and the fully solidified region, in which the solute phase is vitrified. We quantify anisotropic ice crystal growth velocities, obtain structure-processing correlations, and observe at high spatio-temporal resolution phenomena, such as ice crystal instability formation, tip splitting, and the ice templating of cell wall surface features, such as "ridges", "jellyfish caps", and "tentacles."

5. Experimental Section

Preparation of Sucrose: Sucrose solutions of 3% w/v were prepared by first thoroughly hand mixing by shaking sucrose (0.3 g, Cascade Biochem Ltd., Reading, UK) with double distilled water (10 ml) in a 50 ml centrifuge tube (polypropylene, PP; Greiner Bio-One GmbH, Frickenhausen, Germany), then outgassing the solutions for at least 1 h in a vacuum oven (Heraeus, Hanau, Germany) at room temperature and 30 mbar to remove bubbles from the solution.

Ex Situ Freeze Casting of Sucrose Scaffold: Sucrose scaffolds were freeze cast from 3% w/v sucrose solutions using a system detailed by Wegst et al. (2010).[5e] Briefly, a polytetrafluoroethylene (PTFE) tube (25.4 mm outer, 20 mm inner diameter, and 500 mm height) was sealed with a copper mold bottom and filled with the solution (12.5 ml) using a syringe. The mold was then placed with its copper bottom on a liquid nitrogen cooled copper cold finger whose temperature was proportional-integral-derivative (PID) controlled. The molds were equilibrated to 4 °C for 10 min before a cooling rate, $\dot{C}$, of either 1 or 10 °C min^{-1} was applied until the mold reached a temperature of −150 °C. The frozen slurries were then demolded with an Arbor press and lyophilized (FreeZone 6 Plus, Labconco, Kansas City, MO, USA) for 72 h at 0.008 mbar and a coil temperature of −85 °C.

Miniature Freeze Casting System: For the in situ freeze casting experiments, a miniature, lightweight freeze casting system was custom-designed and manufactured (Figure 1). It consists of a copper cold finger chilled by a Cryojet5 (Oxford Instruments, NanoScience, Oxford, UK) set to a temperature of 230 K (−43.15 °C), monitored by a K–type thermocouple (TC Direct, Mönchengladbach, Germany) inserted into the center of the copper cold finger. The 2 mm diameter copper cold finger was designed to securely hold 30 mm long, 2 mm inner diameter Kapton tubes (Goodfellow, Huntingdon, UK) with a perfect seal so, that the 3% w/v sucrose sample solution could be injected directly into the Kapton tube mold using a 1 ml Luer-Lok Tip syringe (Becton, Dickinson and Company, Franklin Lakes, NJ, USA) equipped with a 20 Gauge (0.908 mm outer diameter), 38.1 mm (1.5 inch) long industrial dispensing tip (CML Supply LLC, Lexington, Kentucky, USA). For thermal insulation and draft protection, a 4 mm inner diameter, 60 mm long Kapton tube (Goodfellow, Huntingdon, UK) was secured on the 4 mm diameter portion of the cold finger. This new, custom-designed, and rotationally symmetric miniature in situ freeze-casting system maintained a very precise alignment of the rotation axis. The time-to-angle stability was ensured by the rotation stage controller. A rotational symmetric design was helpful to maintain accuracy. With this setup up to 20 tps could be acquired continuously during the solidification process, with a 180° rotation required for each tomogram.

Local Cooling Rate, $\dot{C}$, and Temperature Gradient, G, Measurements with a Thermocouple Mold: A custom-made thermocouple (TC) mold was manufactured by inserting 0.5 mm wire diameter *T*-type thermocouples (TC Direct, Mönchengladbach, Germany) at 2 mm intervals along the 2 mm inner diameter Kapton tube with the first TC placed at 0 mm mold height, *H*, thus directly onto the cold finger surface. The time-temperature curve of each thermocouple was recorded during the freeze casting of a

3% w/v sucrose sample solution. The time points at which the 0 °C isotherm reached each probe and height were determined. From this time, temperature, and height data the freezing front velocity was calculated. The local cooling rate, $\dot{C}$, for each TC position was determined from the 0 °C to −1 °C temperature-time gradient. To calculate a local cooling rate, $\dot{C}$, and thermal gradient, G, for each mold height, H, an exponential decay function was fitted to the local cooling rate versus probe position curve (Figure S4, Supporting Information).

Tomoscopy: The term tomoscopy was reintroduced for time-resolved studies performed with the explicit aim to explore in 3D the dynamics of structure formation in materials.[9] The name was derived in analogy to the term radioscopy, which is time-resolved radiography. Synchrotron X-ray tomoscopy was performed at the TOMCAT beamline of the Swiss Light Source (SLS), Paul Scherrer Institute (PSI), Switzerland, which is dedicated to time-resolved X-ray imaging.[23]

The polychromatic beam generated by a 2.9 T superconducting bending magnet was reduced in size, with the beamline front end slits, to a field of view of 2.5 × 2.7 mm^2 at the sample position. The bottom of the field of view was 1.94 mm above the top of the copper cold finger. To limit the heat load on both the sample and the detector system, while maintaining a high photon flux at higher X-ray energies, the lower energies of the beam were reduced in intensity with a 1.525 mm thick single crystalline Si wafer and a stack of eight 1 mm thick borosilicate microscope slides. The maximum of the resulting energy spectrum thus shifted to >30 keV. Edge effects were avoided using samples that were at least 10–100 times larger in size than the features of interest. Typical freezing front velocities of 5–30 µm s^{-1} and resulting feature sizes in the range of 10–200 µm,[6b,c,10,15,24] a sample diameter of 2 mm, and a tomoscopy rate of at least one tomogram per second (tps) ensured high-resolution datasets with a voxel size of 2.75 × 2.75 × 2.75 $µm^3$.

The X-ray intensities transmitted and propagated through the sample were collected at a distance of 235 mm and converted into visible light by a 150 µm-thick LuAG:Ce scintillator (CRYTUR, spol. s r.o., Turnov, Czech Republic), guided and magnified with a High Numerical Aperture White-Beam Macroscope (Optique Peter, Lentilly, France)[25] to the CMOS detector of the GigaFRoST high-speed camera[26] providing an image of 912 × 980 pixels, with an effective pixel size of 2.75 × 2.75 $µm^2$ and a measured resolution of 6 µm.[9] One effect to consider, which could adulterate the results in the case of tomoscopy was centrifugal forces. With a radial acceleration of $a = 4\pi^2 f^2 r$, and a rotation frequency of $f = 1$ Hz, the acceleration at the inside of the 1 mm radius Kapton tube (outer part of the sample) would be $a = 0.04$ m $s^{-2} \approx 0.004$ g (gravitational acceleration $g = 9.81$ m s^{-2}), which was negligible, so that the sample rotation during freezing was not expected to cause artifacts during solidification.

Data Acquisition and Processing: The tomoscopic experiments were performed at 1 tps, rotating the sample at 1 Hz and recording a tomogram each second with a total of 500 projections over 180° and an exposure time of ≈1 ms per projection. The images collected by the GigaFRoST high-speed camera were transferred via eight parallel fiber-optical data connections to a backend server with transfer rates of ≈8 GB s^{-1} and written, in parallel, to a high-performance file system.[26] A live preview of the experiment allowed to monitor the evolution of the sample, acting as a simulated radioscopy during the evolution of the experiment, so that the process parameters could be adjusted ad controlled during the experiment, if necessary.

The acquired projections were first filtered with a single-distance propagation-based phase contrast algorithm[27] with a δ/β-ratio of 100 at a propagation distance of 235 mm, and then reconstructed using the gridrec algorithm.[28] The motion of the solidification front was tracked along the vertical z-axis, with the region horizontally divided into patches and the solid-liquid interface being defined as the location of the intensity transition from the solidified to the still liquid phase.

Segmentation of the different phases was performed using a simple threshold approach. A single lamella was selected, using a classical watershed algorithm on the ultimate binarized volume. The lamella was first selected manually and then dilated to create a mask, which was then applied to all binarized volumes of the imaging sequence. Morphological filters were used to remove components of no interest, such as the liquid phase, for example.

The local thickness of ice crystals was calculated after segmentation using the ImageJ plugin "LocalThickness",[29] whereas the mean local thickness was calculated by averaging the obtained values over each horizontal slice of the volume along the z-axis. The horizontal in-plane orientation of the lamellae was quantified using the ImageJ plugin package OrientationJ.[30] In this process, local orientations were calculated using the structure tensor of the input image and displayed for its respective location.[31] The spatial extent of the ice crystal was determined by principal component analysis on the segmented individual lamella. 3D views were generated using either ImageJ, Dragonfly (version 2021.1, Object Research Systems, Montreal, Canada) or Avizo (version 9.0.1, Thermo Fischer, Waltham, USA).

Desktop Tomography: The ex situ freeze-cast sucrose scaffolds were imaged by a desktop X-ray microtomography system (Skyscan 1272, Bruker, Kontich, Belgium), operating at a source voltage and current of 50 kV and 200 µA, respectively. The 360° scans were performed with a step size of 0.1°. The acquired projections of 2940 × 3280 pixels with an effective pixel size of 1.5 × 1.5 $µm^2$ resulted in a horizontal area of 4.4 × 4.4 mm^2 and a vertical height of 4.9 mm. The automatic oversized scan was performed to stack in the vertical direction and cover the entire height of the scaffold (≈32 mm). Reconstructions and visualizations were obtained with the NRecon (version 1.6.9.8, Bruker, Kontich, Belgium) and CTVox software (version 3.0.0, Bruker, Kontich, Belgium). Lamellar spacing and cell wall feature sizes were measured with Fiji (version 1.53f51) at the scaffold heights of 10 and 30.5 mm.

Statistical Analysis: Statistical analysis was performed where possible. The main experiment consisted of one sample being imaged a total of 270 times in successive scans. This allowed data processing in multiple dimensions, such as three spatial directions and time, as illustrated by the following example. To determine the height of the solidification front, the cylindrical sample was first divided into 379 columns of 980 pixels total height, which corresponds to the tomographic volume height. Each of the 980 elements of each column had a square cross-section with an area of 32 × 32 pixels and was first represented by its median grey value, then normalized by the initial grey value of the same element at $t = 0$ s. In the vertical direction, each column was smoothed with a 9 × 1 median filter. The transition from solid to liquid was defined as the maximum negative grey value gradient. Then, a median value was calculated for the entire solidification front across all 379 columns and plotted in Figure 2b, using for the error the standard deviation with respect to the mean value. To obtain the freezing front velocity, the first derivative with respect to time was calculated from the freezing front progression. Finally, a Savitzky-Golay smooth filter was applied with a polynomial order of 2 and a window size of 5.

Supporting Information

Supporting Information is available from the Wiley Online Library or from the author.

Acknowledgements

P.H.K. and K.Y. contributed equally to this work. The authors thank Dwayne B. Adams, Department of Physics, Dartmouth College, for the expert manufacture of the in situ cold finger, and the Core Facility "Imaging of Materials Systems" and Dr. Yi Thomann of the Freiburg Center for Interactive Materials and Bioinspired Technologies for their imaging support. The authors gratefully acknowledge financial support through NASA Awards 80NSSC18K0305 and 80NSSC21K0039, the DFG Reinhart-Koselleck Project 408321454, Ba 1170/40, and BMBF Award 05K18KTA. K.Y. thanks the Alexander von Humboldt Foundation for a Humboldt Research Fellowship. We acknowledge the Paul Scherrer Institute, Villigen, Switzerland for the provision of synchrotron radiation beamtime at the TOMCAT beamline X02DA of the SLS and would like to thank Gordan

Mikuljan and Philipp Zuppiger for technical assistance and Philipp Zuppiger for technical assistance. An additional NASA grant was added to the Acknowledgements on November 23, 2023 after initial online publication.

Conflict of Interest

The authors declare no conflict of interest.

Data Availability Statement

The data that support the findings of this study are available in the supplementary material of this article.

Keywords

anisotropic crystals growth, cell wall surface features, freeze casting, hierarchical architectures

Received: April 28, 2023
Revised: June 28, 2023
Published online: August 18, 2023

[1] a) K. Araki, J. W. Halloran, *J. Am. Ceram. Soc.* **2004**, *87*, 1859; b) K. Araki, J. W. Halloran, *J. Am. Ceram. Soc.* **2005**, *88*, 1108; c) B.-H. Yoon, Y.-H. Koh, C.-S. Park, H.-E. Kim, *J. Am. Ceram. Soc.* **2007**, *90*, 1744; d) M. Naviroj, S. Miller, P. Colombo, K. Faber, *J. Eur. Ceram. Soc.* **2015**, *35*, 2225.

[2] D. Schumacher, M. Wilhelm, K. Rezwan, *Mater. Des.* **2018**, *160*, 1295.

[3] P. H. da Rosa Braun, K. Rezwan, M. Wilhelm, *Mater. Des.* **2021**, *212*, 110186.

[4] K. Araki, J. W. Halloran, *J. Am. Ceram. Soc.* **2004**, *87*, 2014.

[5] a) S. Deville, E. Saiz, R. K. Nalla, A. P. Tomsia, *Science* **2006**, *311*, 515; b) G. Ezekwo, H.-M. Tong, C. C. Gryte, *Water Res.* **1980**, *14*, 1079; c) K. L. Scotti, D. C. Dunand, *Prog. Mater. Sci.* **2018**, *94*, 243; d) U. G. K. Wegst, H. Bai, E. Saiz, A. P. Tomsia, R. O. Ritchie, *Nat. Mater.* **2015**, *14*, 23; e) U. G. K. Wegst, M. Schecter, A. E. Donius, P. M. Hunger, *Philos. Trans. R. Soc., A* **2010**, *368*, 2099.

[6] a) P. Divakar, J. Reeves, J. Gong, F. W. Kolling, P. Jack Hoopes, U. G. K. Wegst, *Acta Biomater.* **2022**, *138*, 342; b) P. Divakar, K. Yin, U. G. K. Wegst, *Data Brief* **2019**, *22*, 502; c) P. Divakar, K. Yin, U. G. K. Wegst, *J. Mech. Behav. Biomed. Mater.* **2019**, *90*, 350; d) K. Yin, P. Divakar, J. Hong, K. L. Moodie, J. M. Rosen, C. A. Sundback, M. K. Matthew, U. G. K. Wegst, *MRS Adv.* **2018**, *3*, 1677; e) K. Yin, P. Divakar, U. G. K. Wegst, *Biomacromolecules* **2019**, *20*, 3733; f) K. Yin, P. Divakar, U. G. K. Wegst, *Acta Biomater.* **2019**, *84*, 231.

[7] a) Y. Cui, H. Gong, Y. Wang, D. Li, H. Bai, *Adv. Mater.* **2018**, *30*, 1706807; b) B. Delattre, R. Amin, J. Sander, J. D. Coninck, A. P. Tomsia, Y.-M. Chiang, *J. Electrochem. Soc.* **2018**, *165*, A388; c) K. Qiu, U. G. K. Wegst, *Adv. Funct. Mater.* **2022**, *32*, 2105635.

[8] a) K. Yin, K. Ji, L. S. Littles, R. Trivedi, A. Karma, U. G. K. Wegst, *Proc. Natl. Acad. Sci. USA* **2023**, *120*, 2210242120; b) B. W. Riblett, N. L. Francis, M. A. Wheatley, U. G. K. Wegst, *Adv. Funct. Mater.* **2012**, *22*, 4920.

[9] a) F. Garcia-Moreno, P. H. Kamm, T. R. Neu, F. Bulk, R. Mokso, C. M. Schlepütz, M. Stampanoni, J. Banhart, *Nat. Commun.* **2019**, *10*, 3762; b) F. Garcia-Moreno, P. H. Kamm, T. R. Neu, F. Bulk, M. A. Noack, M. Wegener, N. von der Eltz, C. M. Schlepütz, M. Stampanoni, J. Banhart, *Adv. Mater.* **2021**, *33*, 2104659; c) P. H. Kamm, T. R. Neu, F. García-Moreno, J. Banhart, *Acta Mater.* **2021**, *206*, 116583.

[10] A. E. Donius, R. W. Obbard, J. A. Burger, P. M. Hunger, I. Baker, R. D. Doherty, U. G. K. Wegst, *Mater. Charact.* **2014**, *93*, 184.

[11] a) D. Girlich, H.-D. Lüdemann, C. Buttersack, K. Buchholz, *Z. Naturforsch., C: Biosci.* **1994**, *49*, 258; b) A. Heinrich-Schramm, C. Buttersack, H.-D. Lüdemann, *Carbohydr. Res.* **1996**, *293*, 205; c) M. Rampp, C. Buttersack, H.-D. Lüdemann, *Carbohydr. Res.* **2000**, *328*, 561; d) B. Zobrist, V. Soonsin, B. P. Luo, U. K. Krieger, C. Marcolli, T. Peter, T. Koop, *Phys. Chem. Chem. Phys.* **2011**, *13*, 3514.

[12] K. Yin, K. Ji, L. S. Littles, R. Trivedi, A. Karma, U. G. K. Wegst, *Proc. Natl. Acad. Sci. USA* **2023**, *120*, 2210242120.

[13] O. Betz, U. G. K. Wegst, D. Weide, M. Heethoff, L. Helfen, W.-K. Lee, P. Cloetens, *J. Microsc.* **2007**, *227*, 51.

[14] D. Fisher, M. Rappaz, W. Kurz, *Fundamentals of Solidification*, 5th fully revised ed.,Trans Tech Publications Ltd, Baech, Switzerland **2023**,pp. 1–353.

[15] K. Yin, P. Divakar, U. G. K. Wegst, *J. Mech. Behav. Biomed. Mater.* **2021**, *121*, 104589.

[16] P. M. Hunger, A. E. Donius, U. G. K. Wegst, *J. Mech. Behav. Biomed. Mater.* **2013**, *19*, 87.

[17] S. Deville, E. Maire, A. Lasalle, A. Bogner, C. Gauthier, J. Leloup, C. Guizard, *J. Am. Ceram. Soc.* **2009**, *92*, 2489.

[18] a) M. Marcellini, C. Noirjean, D. Dedovets, J. Maria, S. Deville, *ACS Omega* **2016**, *1*, 1019; b) D. Dedovets, S. Deville, *J. Eur. Ceram. Soc.* **2018**, *38*, 2687; c) D. Dedovets, C. Monteux, S. Deville, *Ultramicroscopy* **2018**, *195*, 1.

[19] A. Bareggi, E. Maire, A. Lasalle, S. Deville, *J. Am. Ceram. Soc.* **2011**, *94*, 3570.

[20] H. Nada, Y. Furukawa, *J. Cryst. Growth* **2005**, *283*, 242.

[21] a) K. Yin, P. Divakar, U. G. K. Wegst, *J. Mech. Behav. Biomed. Mater.* **2023**, *121*, 104589; b) T. Waschkies, R. Oberacker, M. J. Hoffmann, *J. Am. Ceram. Soc.* **2009**, *92*, S79.

[22] a) K. Yin, M. D. Mylo, T. Speck, U. G. K. Wegst, *J. Mech. Behav. Biomed. Mater.* **2020**, *110*, 103826; b) K. Yin, M. D. Mylo, T. Speck, U. G. K. Wegst, *Data Brief* **2020**, *31*, 105870; c) M. Kuberka, D. Von Heimburg, H. Schoof, I. Heschel, G. Rau, *Int. J. Artif. Organs* **2002**, *25*, 67; d) H. Tong, I. Noda, C. C. Gryte, *Colloid Polym. Sci.* **1984**, *262*, 589.

[23] M. Stampanoni, A. Groso, A. Isenegger, G. Mikuljan, Q. Chen, A. Bertrand, S. Henein, R. Betemps, U. Frommherz, P. Böhler, D. Meister, M. Lange, R. Abela, *Proc. SPIE 6318, Developments in X-Ray Tomography V*, SPIE, San Diego, California, United States **2006**, https://doi.org/10.1117/12.679497 (accessed: September 2006).

[24] a) A. E. Donius, A. Liu, L. A. Berglund, U. G. K. Wegst, *J. Mech. Behav. Biomed. Mater.* **2014**, *37*, 88; b) P. M. Hunger, A. E. Donius, U. G. K. Wegst, *Acta Biomater.* **2013**, *9*, 6338.

[25] M. Bührer, M. Stampanoni, X. Rochet, F. Büchi, J. Eller, F. Marone, *J. Synchrotron Radiat.* **2019**, *26*, 1161.

[26] R. Mokso, C. M. Schlepütz, G. Theidel, H. Billich, E. Schmid, T. Celcer, G. Mikuljan, L. Sala, F. Marone, N. Schlumpf, *J. Synchrotron Radiat.* **2017**, *24*, 1250.

[27] D. Paganin, S. C. Mayo, T. E. Gureyev, P. R. Miller, S. W. Wilkins, *J. Microsc.* **2002**, *206*, 33.

[28] B. A. Dowd, G. H. Campbell, R. B. Marr, V. V. Nagarkar, S. V. Tipnis, L. Axe, D. P. Siddons, *Proc. SPIE 3772, Developments in X-Ray Tomography II*, SPIE, Bellingham, WA **1999**, (accessed: September 1999), pp. 224–236.

[29] R. Dougherty, K.-H. Kunzelmann, *Microsc. Microanal.* **2007**, *13*, 1678.

[30] a) J. Schindelin, I. Arganda-Carreras, E. Frise, V. Kaynig, M. Longair, T. Pietzsch, S. Preibisch, C. Rueden, S. Saalfeld, B. Schmid, *Nat. Methods* **2012**, *9*, 676; b) Z. Püspöki, M. Storath, D. Sage, M. Unser, in *Focus on Bio-Image Informatics* (Eds: W. De Vos, S. Munck, J. P. Timmermans), Springer, Cham **2016**, *219*, pp. 69.

[31] T. Hildebrand, P. Rüegsegger, *J. Microsc.* **1997**, *185*, 67.